

Predicting band structure of 3D mechanical metamaterials with complex geometry via XFEM

Jifeng Zhao · Ying Li · Wing Kam Liu

Received: 14 November 2014 / Accepted: 3 February 2015 / Published online: 20 February 2015
© Springer-Verlag Berlin Heidelberg 2015

Abstract Band structure characterizes the most important property of mechanical metamaterials. However, predicting the band structure of 3D metamaterials with complex microstructures through direct numerical simulation (DNS) is computationally inefficient due to the complexity of meshing. To overcome this issue, an extended finite element method (XFEM)-based method is developed to predict 3D metamaterial band structures. Since the microstructure and material interface are implicitly resolved by the level-set function embedded in the XFEM formulation, a non-conforming (such as uniform) mesh is used in the proposed method to avoid the difficulties in meshing complex geometries. The accuracy and mesh convergence of the proposed method have been validated and verified by studying the band structure of a spherical particle embedded in a cube and comparing the results with DNS. The band structures of 3D metamaterials with different microstructures have been studied using the proposed method with the same finite element mesh, indicating the flexibility of this method. This XFEM-

based method opens new opportunities in design and optimization of mechanical metamaterials with target functions, e.g. location and width of the band gap, by eliminating the iterative procedure of re-building and re-meshing microstructures that is required by classical DNS type of methods.

Keywords XFEM · Phononic band gap · Bloch wave analysis · Mechanical metamaterials · Parallel computing

1 Introduction

Metamaterials are artificial materials engineered to have exceptional optical, thermal, electromagnetic or mechanical properties not found in nature. For example, the traditional materials encountered in optics, e.g. water and glass, are characterized with both positive permittivity and permeability leading a positive refractive index. When the light passes from a fast medium (such as vacuum) to a slow medium (such as glass), it will bend toward the normal to the boundary between these two media. Since the refractive index of glass is positive, the rays will be refracted on the *other* side of the normal upon entering the glass. On the contrary, optical metamaterials can be engineered to have both negative permittivity and permeability [60], meaning the refraction index n of these materials will be negative. Therefore when the light wave propagates from one medium to another one, it will be refracted on the *same* side of the normal upon entering the material. The extraordinary negative refractive index allows us to be able to fabricate the superlens with resolution beyond the diffraction limit [17, 44] and even cloaking devices [8, 66]. We should emphasize that, to date, all of the materials with negative refractive index are artificially engineered materials [16]. These metamaterials are assemblies of multiple individual elements made of conventional materials, e.g. metals

J. Zhao
Theoretical & Applied Mechanics, Northwestern University,
Evanston, IL, USA
e-mail: jifengzhao2015@u.northwestern.edu

Y. Li · W.K. Liu (✉)
Department of Mechanical Engineering, Northwestern University,
Evanston, IL, USA
e-mail: w-liu@northwestern.edu

Y. Li
e-mail: yingli@u.northwestern.edu

W. K. Liu
Distinguished Scientists Program Committee, King Abdulaziz
University (KAU), Jeddah, Saudi Arabia

or plastics, but they are arranged in periodic spatial patterns in their respective microstructures.

Similar to optical metamaterials, mechanical or acoustic metamaterials can also have a negative index of refraction. In acoustic metamaterials, sonic waves can be directed and manipulated through the bulk modulus K and density ρ , which are analogs of permittivity and permeability. When K and ρ are both negative, the materials will have negative refractive index with potential applications including acoustic cloaking [9], superlensing [1], and energy absorption [20,32,41,64].

The phononic band structure, in direct analogy to photonic band structure of electromagnetic materials, characterizes the most important property of mechanical metamaterials. For instance, the mechanical metamaterials can behave like solids or liquids with negative dispersion bands if both the modulus and density of these materials are negative within a specific frequency range [30,39]. Most importantly, the wave cannot propagate through the structure certain frequency ranges or wavelengths, resulting in the ‘band gaps’ in the band structure. The periodic variations of the density and/or elastic modulus of the constituents in these mechanical metamaterials change the speed of sound, which in turn leads to a band gap. The band gap can be used to realize a number of applications including effective waveguiding, wave transduction and non-destructive detection [53].

Numerous theoretical and numerical methodologies have been developed and combined to predict the band structure of these metamaterials [24]. Bloch theory paves the theoretical foundations of band structure analysis and has been applied on a single unit cell of the periodic structure in the reciprocal lattice space (Brillouin zone) [28]. To numerically predict the band structure, planewave expansion (PWE) method [31,37,56,58], finite difference time domain (FDTD) method [45,52], multiple scattering theory (MST) [7,29,36], and finite element method (FEM) [2,14] are commonly used. Among them, FEM is the most widely used since it has demonstrated relatively high computational efficiency, accuracy with a fast convergence rate. However, in studying 3D mechanical metamaterials with substantial geometric complexity, e.g. pentamode metamaterials [39,42], creating and meshing the geometric model in traditional FEM still suffer from considerable computational burdens. Therefore, to date, most of the studies on the band structures of these metamaterials are limited to 2D with simple geometries. More importantly, in the design and topology optimization process of 3D metamaterials, it is required to iteratively re-build and re-mesh complex microstructures which leads to unacceptable computational expenses in traditional FEM. Therefore, the design and optimization of 3D metamaterials with target functions (such as band structures) is still a forbidden challenge for traditional FEM [40,57].

To overcome the aforementioned challenges and provide an efficient way to predict the band structure of 3D metamaterials with complex microstructures, we use the extended finite element method (XFEM) [15], as opposed to the traditional FEM, to *implicitly* account for the complex geometries of different constituents in the metamaterials. The XFEM is developed to overcome the difficulties in solving problems with localized features which cannot be efficiently solved by mesh refinement. In the XFEM, the standard polynomial basis functions (shape functions) are augmented by discontinuous basis functions to account for material interfaces for the elements that are shared by different materials with different mechanical properties [43]. A key advantage of XFEM is that the finite element mesh does not need to be updated to track the evolving discontinuities in such problems. Therefore, XFEM is naturally suitable for designing and optimizing 3D metamaterials with complex microstructures by avoiding re-meshing during the process. Here we should emphasize that other numerical methods exist to handle the complex geometries of the microstructures, e.g. moving least-squares method [26,27,35], conforming local meshfree method [55] and isogeometric analysis [11,12,23]. However, microstructure re-building and re-meshing procedure is still unavoidable in these methods when applied to optimization problems, which makes XFEM a more appealing candidate in design and optimization of 3D metamaterials.

Sukumar and Pask [54] have explored the possibility of incorporating Bloch-periodic boundary condition into the enriched finite element method by modifying the local classical shape functions and partition-of-unity enrichment functions. In their work, the enrichment is added to solve quantum-mechanical quantities, such as charge density, in Poisson and Schrödinger equations. Different than the previous study [54], enriched degrees of freedom in present work represent the real microstructure in multiple-phase metamaterials. Bloch-periodic boundary conditions will be applied through kinetic constraints without further modification of both classical and enriched shape functions in our formulation.

The organization of the paper will now be discussed. In Sect. 2, we describe the methodology for calculating the band structure of 3D metamaterials based on XFEM. A parallelized and efficient method for solving the tremendous number of degrees of freedom in the system is also presented in Sect. 2. Section 3 will show a comparison of the results from XFEM with direct numerical simulations (DNS), illustrating the mesh convergence and flexibility of the proposed method. The band structures of different 3D metamaterials obtained through XFEM simulations and a discussion of the different underlying physical mechanisms will be presented in Sect. 4. Conclusions are drawn in Sect. 5.

2 Methodology

2.1 Bloch–Floquet wave analysis

According to the classical Bloch–Floquet theorem [28], all fields in an infinite periodic solid can be expanded to infinite bases

$$h(\mathbf{x}, t) = \sum_{\mathbf{K}} h_{\mathbf{K}}(\omega, \mathbf{K}) \exp[i(\omega t - \mathbf{K} \cdot \mathbf{x})] \quad (1)$$

where h is any mechanical field such as stress or displacement, \mathbf{K} is the Bloch–Floquet wave vector, the latter of which represents the spatial frequency. Therefore, in response to a given incident wave \mathbf{K} , the displacement field (for example) in a solid body will be

$$\mathbf{u}(\mathbf{x}, t) = \bar{\mathbf{u}}_{\mathbf{K}}(\omega, \mathbf{K}) \exp[i(\omega t - \mathbf{K} \cdot \mathbf{x})] \quad (2)$$

where $\bar{\mathbf{u}}_{\mathbf{K}}(\omega, \mathbf{K})$ is the magnitude of displacement field depending on wave vector \mathbf{K} and frequency ω .

2.2 Governing equation

The equation of motion for a deformed solid body is represented by the conservation of linear momentum [6], by assuming absence of any body force,

$$\nabla \cdot \sigma = \rho \frac{D^2 \mathbf{x}}{Dt^2} \quad (3)$$

Due to the periodicity of metamaterials, the displacement field should follow the Bloch wave equation (Eq. 2). Substituting Eq. 2 into Eq. 3, we obtain

$$\nabla \cdot \sigma + \rho \omega^2 \mathbf{u} = 0 \quad (4)$$

2.3 Periodic boundary condition

A solid body with an infinite periodic structure can be characterized by its unit cell and corresponding translation vectors

$$\mathbf{T} = n_i \mathbf{a}_i \quad (5)$$

where n_i is arbitrary integer while \mathbf{a}_1 , \mathbf{a}_2 , and \mathbf{a}_3 are translation vectors. In this way, the microstructure in a unit cell is repeated periodically under a translation $\Delta \mathbf{x} = \mathbf{T}$.

The spatial periodicity allows us to only model the unit cell with proper periodic boundary conditions. Assuming the displacement field follows the Bloch wave equation (Eq. 2), the displacement after a spatial translation is described by

$$\mathbf{u}(\mathbf{x} + \mathbf{T}, t) = \bar{\mathbf{u}}_{\mathbf{K}}(\omega, \mathbf{K}) \exp[i(\omega t - \mathbf{K} \cdot (\mathbf{x} + \mathbf{T}))] \quad (6)$$

Substituting Eq. 2 into Eq. 6, boundary conditions for the unit cell are obtained as

$$\mathbf{u}(\mathbf{x} + \mathbf{T}, t) = \mathbf{u}(\mathbf{x}, t) \exp(i\mathbf{K} \cdot \mathbf{T}) \quad (7)$$

In Eq. 7, we are only interested in the wave vectors \mathbf{K} that lay on the boundary of the irreducible Brillouin zone in the reciprocal space. For a detailed introduction on reciprocal lattice space and reciprocal vectors, readers are referred to the Appendix 1 and Ref. [47].

The complex-valued boundary problem in Eq. 7 needs to be rearranged in order to be solved in a real space. The displacement fields $\mathbf{u}(\mathbf{x} + \mathbf{T})$ and $\mathbf{u}(\mathbf{x})$ can be written in a complex space:

$$\mathbf{u} = \mathbf{u}_{\text{re}} + i\mathbf{u}_{\text{im}} \quad (8)$$

where the subscripts ‘re’ and ‘im’ represent the displacement in the real and imaginary spaces, respectively. Substituting Eq. 8 into Eq. 7, boundary conditions can be re-written as

$$\begin{aligned} \mathbf{u}_{\text{re}}(\mathbf{x} + \mathbf{T}, t) &= \mathbf{u}_{\text{re}}(\mathbf{x}, t) \cos(\mathbf{K} \cdot \mathbf{T}) - \mathbf{u}_{\text{im}}(\mathbf{x}, t) \sin(\mathbf{K} \cdot \mathbf{T}) \\ \mathbf{u}_{\text{im}}(\mathbf{x} + \mathbf{T}, t) &= \mathbf{u}_{\text{re}}(\mathbf{x}, t) \sin(\mathbf{K} \cdot \mathbf{T}) + \mathbf{u}_{\text{im}}(\mathbf{x}, t) \cos(\mathbf{K} \cdot \mathbf{T}) \end{aligned} \quad (9)$$

where \mathbf{u}_{re} and \mathbf{u}_{im} are two uncoupled fields in the real space which satisfy the same governing equation:

$$\begin{aligned} \nabla \cdot \sigma_{\text{re}} + \rho \omega^2 \mathbf{u}_{\text{re}} &= 0 \\ \nabla \cdot \sigma_{\text{im}} + \rho \omega^2 \mathbf{u}_{\text{im}} &= 0 \end{aligned} \quad (10)$$

Therefore, the above equation (Eq. 10) can be solved by two identical finite element meshes constrained by proper boundary conditions defined by Eq. 9. The two equations in Eq. 10 are fully coupled because of the applied constraints in Eq. 9, leading to the appearance of off-diagonal entries in the stiffness and mass matrices during the finite element discretization, as a by-product of any periodic system. This will dramatically increase the complexity and difficulty in solving the final eigenvalue problem, which will be discussed in detail in Sect. 2.5.

2.4 Finite element discretization

The unit cell is discretized and solved by using the FEM, according to the governing equations mentioned in the previous section. However, the conventional DNS method requires a conforming mesh to *explicitly* resolve the geometric boundaries between different materials, limiting the potential of the method in application to complex geometric boundaries that are difficult to mesh. In this study, XFEM [43] is adopted to *implicitly* resolve these material interfaces (microstructures) which does not require a conforming mesh (a uniform mesh is used in our case). The information of the complex microstructure is restored by the combination of a level-set function and an enriched field given by the XFEM formulation. Therefore, the proposed method is suitable for modeling mechanical metamaterials with different complex microstructures by avoiding the necessity of changing finite element meshes.

The displacement field in XFEM is enriched by additional degrees of freedom and represented by enrichment functions:

$$\mathbf{u}^h(\mathbf{x}) = \sum_{I \in \Lambda} N_I(\mathbf{x}) \mathbf{u}_I + \sum_{J \in \Sigma} N_J(\mathbf{x}) \psi_J(\mathbf{x}) \mathbf{a}_J \quad (11)$$

where Λ is the set of all nodes in the finite element mesh, $\Sigma \in \Lambda$ is the subset of nodes that are enriched by discontinuities, N_J are the shape functions, $\psi_J(\mathbf{x})$ is the enrichment function, and \mathbf{a}_J are the additional degrees of freedom at node J . Through the flexibility in choosing the enrichment function $\psi_J(\mathbf{x})$, the solution can represent many different types of fields including cracks and material interfaces. In the present work, weak discontinuities will be considered to represent the perfectly bonded material interface. Here ψ_J^w is defined by

$$\psi_J(\mathbf{x}) = \psi(\mathbf{x}) = \sum_I N_I(\mathbf{x}) |\phi(\mathbf{x}_I)| - \left| \sum_I N_I(\mathbf{x}) \phi(\mathbf{x}_I) \right| \quad (12)$$

where $\phi(\mathbf{x}_I)$ is the value of a level-set function which is the signed distance function from node \mathbf{x}_I to the material interface. This level-set function therefore implicitly describes the geometric information of the material interface. The enrichment function in Eq. 12 is so-called ‘shifted’ enrichments as suggested by Moës et al. [43], as they possess zero values at nodal positions. Therefore, the additional degrees of freedom will not influence the neighboring elements, and no blending elements are necessary [19]. The subscript of ψ can be omitted since it is a scalar function that does not depend on the node index J . The enrichment function is shifted so that it vanishes at the edges of the elements that are not intersected by the material interface. $\psi_J(\mathbf{x})$ has C^0 continuity across the interface such that it produces a ‘kink’ in the displacement field, and therefore, a jump in the strain field.

Assuming the absence of any body force, the weak form for the momentum equation is

$$\int_{\Omega} \delta u_i \rho \ddot{u}_i d\Omega = \int_{\Gamma_t} \delta u_i \bar{t}_i d\Gamma - \int_{\Omega} \frac{\partial(\delta u_i)}{\partial x_j} \sigma_{ij} d\Omega \quad (13)$$

for $u \in U$ and $\delta u \in V$ where the trial and test functions are defined in the following spaces:

$$U = \{\mathbf{u}(\mathbf{x}, t) | \mathbf{u}(\mathbf{x}, t) \in C^0, \quad \mathbf{u}(\mathbf{x}, t) = \bar{\mathbf{u}}(t) \text{ on } \Gamma^u\} \quad (14)$$

$$V = \{\delta \mathbf{u}(\mathbf{x}, t) | \delta \mathbf{u}(\mathbf{x}, t) \in C^0, \quad \delta \mathbf{u}(\mathbf{x}, t) = 0 \text{ on } \Gamma^u\} \quad (15)$$

The discretized displacement fields are

$$u_i(\mathbf{x}) = \sum_{I \in \Lambda} N_I(\mathbf{x}) u_{iI} + \sum_{J \in \Sigma} N_J(\mathbf{x}) \psi_J(\mathbf{x}) a_{iJ} \quad (16)$$

$$\delta u_i(\mathbf{x}) = \sum_{I \in \Lambda} N_I(\mathbf{x}) \delta u_{iI} + \sum_{J \in \Sigma} N_J(\mathbf{x}) \psi_J(\mathbf{x}) \delta a_{iJ} \quad (17)$$

In the current application, the periodic boundary conditions (Eq. 9) are applied by constraining the kinematic

fields (without kinetic boundary conditions applied explicitly). Therefore, $\bar{\mathbf{t}}$ in Eq. 13 will be omitted in the following portion of the manuscript. Substituting these discretized displacements into the weak form gives the modified Lagrangian equation of motion in discretized form as:

$$(\mathbf{K} - \omega^2 \mathbf{M}) \mathbf{u} = 0 \quad (18)$$

where the stiffness and mass matrices for a single element are

$$\mathbf{K}^e = \begin{bmatrix} \mathbf{K}_{uu}^e & \mathbf{K}_{uu}^e \\ \mathbf{K}_{ua}^e & \mathbf{K}_{aa}^e \end{bmatrix} = \int_{\Omega_e} \begin{bmatrix} \mathbf{B}_{std}^T \mathbf{D} \mathbf{B}_{std} & \mathbf{B}_{enr}^T \mathbf{D} \mathbf{B}_{std} \\ \mathbf{B}_{std}^T \mathbf{D} \mathbf{B}_{enr} & \mathbf{B}_{enr}^T \mathbf{D} \mathbf{B}_{enr} \end{bmatrix} d\Omega_e \quad (19)$$

$$B_{iI}^{std} = \frac{\partial N_I}{\partial x_i} \quad (20)$$

$$B_{iI}^{enr} = \frac{\partial (N_I \psi_I)}{\partial x_i} \quad (21)$$

$$\mathbf{M}^e = \begin{bmatrix} \mathbf{M}_{uu}^e & \mathbf{M}_{uu}^e \\ \mathbf{M}_{ua}^e & \mathbf{M}_{aa}^e \end{bmatrix} = \int_{\Omega_e} \rho \begin{bmatrix} \mathbf{N}_{std}^T \mathbf{N}_{std} & \mathbf{N}_{enr}^T \mathbf{N}_{std} \\ \mathbf{N}_{std}^T \mathbf{B}_{enr} & \mathbf{N}_{enr}^T \mathbf{N}_{enr} \end{bmatrix} d\Omega_e \quad (22)$$

$$N_I^{sta} = N_I \quad (23)$$

$$N_I^{enr} = N_I \psi_I \quad (24)$$

Thus, the above problem has been reduced to an eigenvalue problem with boundary conditions defined by Eq. 9. Note that the mass and stiffness matrices are integrated by standard Gaussian integration with condense integration points, since the subdivision procedure encounters with tremendous implementation difficulties in 3D. Moreover, convergence behaviors have been observed when more than 7 integration points are used in each dimension, indicating that the integration points are dense enough to secure accuracy. The XFEM results will be further validated by comparing with DNS in Sect. 3. The extra computational cost due to the condense integration points is affordable in the current study, because the time for assembling these matrices are nearly negligible comparing to the running time of solving eigenvalue problems. Finally, we should emphasize that when the interface is very close to nodal points so that all the integration points are on the same side of the interface, the standard integration is incapable to precisely capture the interface, therefore only gives approximation.

2.5 Details of implementation

In this study, the problem of interest involves solving a series of eigenvalue problems of large sparse matrices (such as stiffness and mass matrices) with millions of degrees of freedom. Thus, traditional eigenvalue solvers based on a single processor calculation is neither suitable nor applicable for this problem, due to the extensive computational costs. The Portable,

Extensible Toolkit for Scientific Computation (PETSc) package provides an excellent solution to operate on the large sparse matrix in parallel [4]. The sequential and parallel data structure of PETSc for operating on large sparse matrices, including matrix-vector multiplication, matrix factorization, and triangular solving capability, makes it the most successful and widely used parallel numerical package for scientific applications in solving partial differential equations. Built upon PETSc, the Scalable Library for Eigenvalue Problem Computations (SLEPc) provides state-of-the-art algorithms and tools to solve large-scale eigenvalue problems [48]. Herein, we take advantage of both software packages to develop a robust PETSc/SLEPc-based eigenvalue solver suitable for the current problem. The stiffness and mass matrices are constructed by using the standard FEM package then imported into the eigensolver to efficiently calculate the band structure of 3D metamaterials in parallel.

SLEPc offers built-in support for major eigensolvers and preconditioners. The state-of-the-art eigensolvers that are currently available in SLEPc include (i) classical methods such as power iteration, subspace iteration and Rayleigh quotient iteration (RQI); (ii) Krylov methods such as Arnoldi, Lanczos and Krylov–Schur; and (iii) Davidson type iterative eigensolvers including Generalized Davidson and Jacobi–Davidson [49,63]. For more detailed discussion of these solver options, readers are referred to PETSc and SLEPc user manuals [4,48]. In this work, the problem of interest in Eq. 18 is a generalized eigenvalue problem with symmetric and definite matrices. However, the constraints (Eq. 9) between real components and imaginary components, as in Eq. 10, give rise to a substantial amount of non-diagonal entries in the stiffness matrix, making the matrices more ill-conditioned and adding complexity to the solution procedure. We choose to adopt the Krylov–Schur eigensolver which is a variation of Arnoldi eigensolver with a very effective restarting technique for computing eigenvalues in the periphery of the solution spectrum. When coupled with the shift-and-invert spectral transformation technique, it provides a suitable solution for calculating interior eigenvalues. Moreover, choosing the proper matrix preconditioners is essential to reducing computational costs and improving numerical convergence. Here we use the combination of the Block Jacobian (bjacobi) preconditioner and the Incomplete Cholesky (icc) preconditioner, which were found to be the most suitable preconditioners, providing a fast, robust and powerful solution for the current problem. The run-time keyword and other options are summarized in Appendix 2.

3 Method validation and verification

In this section, the accuracy and convergence behavior of the proposed method is tested on a simple cubic crystal by

Table 1 Material constants for SC crystal. E , ρ and ν are the Young's modulus, density and Poisson's ratio of the materials, respectively. c_l and c_t are the longitudinal and transverse speed of sound in the material $c_l = \sqrt{(\lambda + 2G)/\rho}$ and $c_t = \sqrt{G/\rho}$ where λ and G are Lamé first constant and shear modulus determined by E and ν

Materials	E (MPa)	ρ (kg/m ³)	ν	c_l (m/s)	c_t (m/s)
Tungsten	359,059	19.3×10^3	0.188	4514.2	2798
Silastic	17.482	1.3×10^3	0.458	243.9	67.9

comparing the obtained results with DNS. The flexibility of our method for capturing the evolving microstructure is also demonstrated through changing the radius of the embedded spherical particle while maintaining the same finite element mesh.

3.1 Simple cubic (SC) crystal

Here we consider a composite material made of spherical tungsten particles embedded into silastic matrix material in 3D arranged into a SC lattice. The material constants for these two constituents are listed in Table 1. The lattice constant of the SC crystal is $a = 16$ mm with the radius of the sphere set to $r = 5$ mm. The irreducible Brillouin zone of the SC lattice in the reciprocal space is described in Fig. 13 in the Appendix 1 and is enveloped by the path R - M - Γ - X - M . The path is equally divided into 40 wave vectors. For each wave vector, an eigenvalue problem as in Eq. 18 with proper boundary conditions is to be numerically solved by our proposed method.

The finite element meshes for the proposed method and for the DNS calculation of the SC crystal are given in Fig. 1a, b, respectively. As aforementioned, a uniform mesh with 8-nodes cubic element is used in the proposed method, regardless of the particle geometry, since the geometric information (material interface) has already been accounted by the level-set functions (see discussions in Sect. 2.4). Due to the simplicity of the SC crystal, it is also computationally feasible to perform the DNS calculation by the traditional FEM to make a comparison. As will be shown in the following section, the DNS type of simulation will not be feasible when complex microstructures are encountered. The traditional FEM models the material interface by explicitly aligning elements to the particle boundaries. Due to the curved nature of the spherical particle, linear 3D 4-nodes tetrahedron elements must be used which is known to result in a reduction in the convergence rate as compared to the 8-nodes cubic element adopted in the XFEM case. The size of the tetrahedron element has to be reduced dramatically when approaching the material interface in order to accurately capture the high strain gradients. Figure 1 presents a comparison between the DNS mesh and the XFEM mesh while keeping the same mesh seed den-

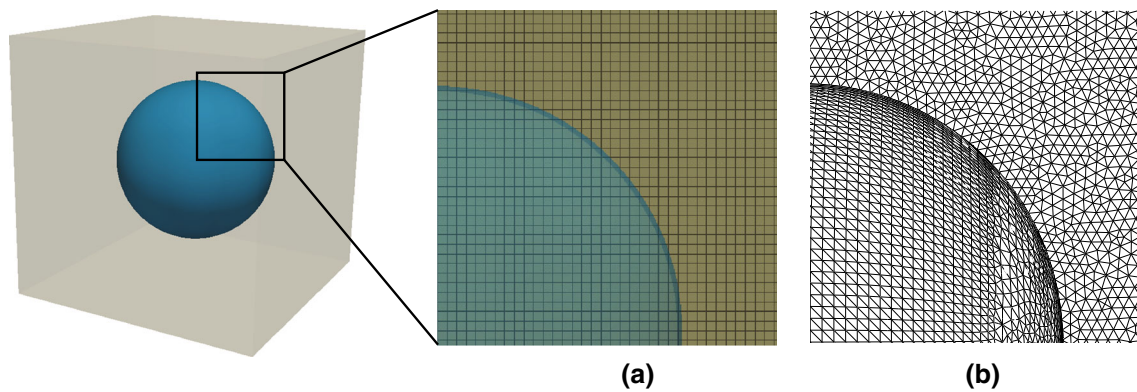


Fig. 1 Comparison between **a** uniform (non-conforming) mesh for XFEM and **b** conforming mesh for traditional FEM

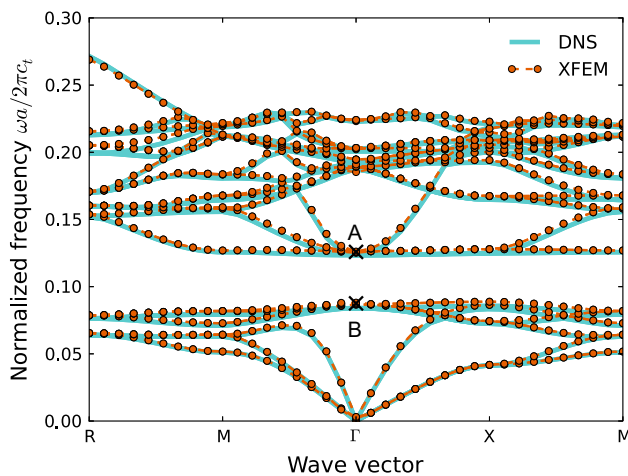


Fig. 2 Band gap structure of simple cubic (SC) crystal predicted by XFEM and DNS calculations

sity. In this example, XFEM calculation actually yields more degrees of freedom than DNS, i.e. 3,188,646 and 1,977,132 for XFEM and DNS, respectively. However, this is mainly induced by the linear elements being used for simplifying the XFEM implementation, leading to the linear approximation of the curved interface. In the future work, high-order elements can be used in the same XFEM framework, which can release the limitation of small element size and reduce the total number of degree of freedom. The advantage of the proposed XFEM framework lies behind the simplicity of generating meshes since uniform mesh is allowed. The benefits are even more profound when dealing with design and optimization problems where iterative re-meshing is required, as the XFEM can resolve the evolving geometries (material interfaces) without updating the meshes.

The frequency of the band structures of the SC crystal predicted by the traditional FEM (DNS) and XFEM are presented in Fig. 2, denoted by solid lines and dots, respectively. The frequency has been normalized to a dimensionless number using the factor $a/2\pi c_t$, where a and c_t are the lattice

Table 2 Mesh sizes for convergence study. $30 \times 30 \times 30$ represents there are 30 elements along the x , y and z directions. Therefore, there are 27,000 elements in total. h_x is the side length of a single element

Number of elements	Mesh size h_x (mm)
$30 \times 30 \times 30$	0.533
$50 \times 50 \times 50$	0.320
$70 \times 70 \times 70$	0.229
$80 \times 80 \times 80$	0.200

constant and transverse wave speed of the matrix material (silastic), respectively. The band structure predicted by the XFEM is in excellent agreement with the result given by DNS, demonstrating the accuracy of the proposed method. To further study the mesh convergence, different mesh sizes, as given in Table 2, are used for the same particle geometry. The relative error is estimated as

$$e_r = \text{abs}(E_{\text{XFEM}} - E_{\text{DNS}})/E_{\text{DNS}}$$

where E_{XFEM} and E_{DNS} are the eigenvalues calculated by the XFEM simulation and DNS, respectively. The results given by DNS are chosen to be the baseline solutions which are considered to be close to the true solutions. Then, we choose the lowest five eigenvalues at point M as representatives to illustrate the convergence rate with respect to the element size, as described in Fig. 3. All of these five eigenvalues converge to the DNS results with rate of 1.5. Moreover, the mode shapes at points A and B in the band structure (see Fig. 2) given by the XFEM simulation are compared with the DNS calculations as presented in Fig. 4. Again, they are in good agreement with each other, which further validates that the proposed method can be used to capture the material interface efficiently.

From the band structure of the SC crystal (cf. Fig. 2), there exists a complete band gap between the normalized frequency 0.08 and 0.125. The propagation of mechanical waves with frequencies in this range is forbidden in the SC

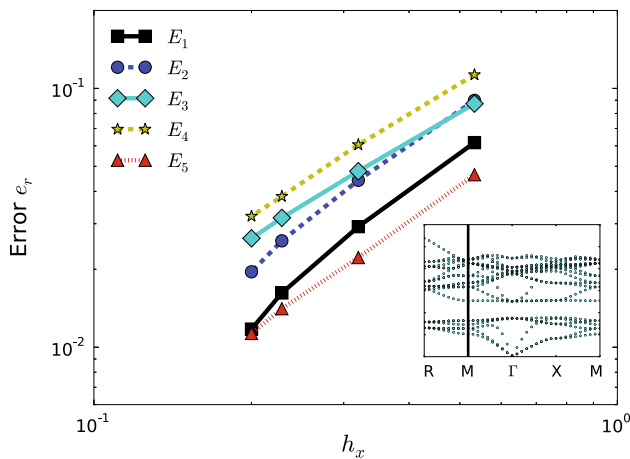


Fig. 3 Mesh convergence of the XFEM. h_x is the element size. E_n denotes the n th lowest eigenvalue at M point (see the *inset* figure)

crystal. The band gap characterizes the most important property of the metamaterials, as discussed in the introduction, and can be accurately determined by our proposed method. This band gap is induced by the Bragg scattering mechanism, due to the periodic 3D space. Typically, the lowest band gap results from scattering of the longitudinal wave and the wave length of the band gap frequency is on the same order of the longitudinal wave length [50,65]. Therefore, the band gap structure is highly related to the size and shape of the crystal, mechanical properties of the different constituents, and the volume fraction of the embedded particle, which will be demonstrated in the following section.

3.2 Volume fraction dependent band gap

The band gap location and its width are dependent on the volume fraction (or filling ratio) of the embedded particle in the SC crystal. We adopt the XFEM to study this effect since the finite element mesh does not need to be updated, as compared to the traditional FEM (DNS). Therefore, the current method is more flexible for modeling different sized/shaped microstructures. The volume fraction of the embedded spherical particle has been increased from 12.8 to 40 %, by increasing its radius from 5 mm to 7.31 mm as given in Table 3. To balance computational cost and accuracy, we use the $70 \times 70 \times 70$ finite element meshes instead of the finest mesh ($80 \times 80 \times 80$). The dependence of the band gap on the volume fraction of the spherical particle is demonstrated in Fig. 5. With increasing particle radius, the location of the band gap frequency and its width have been simultaneously enlarged which has also been observed in previous works [37,59].

With the help of the XFEM formulation, the geometry of the embedded particle can be represented by a pre-defined level-set function, while the finite element meshes

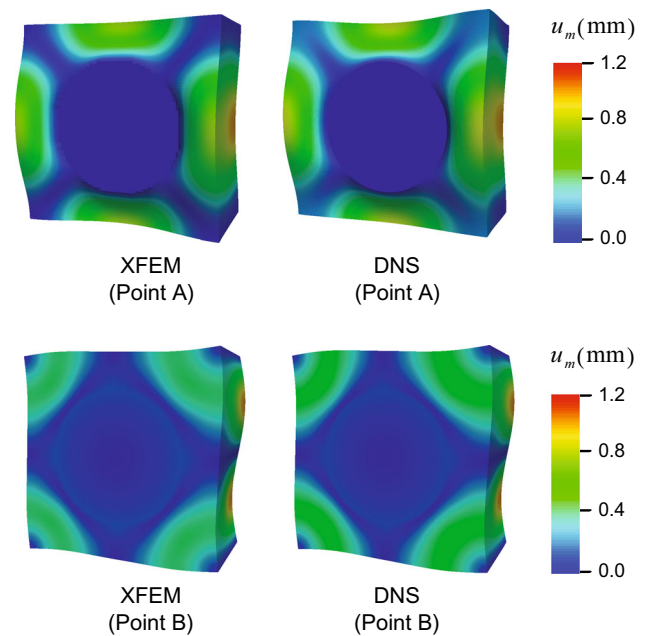


Fig. 4 Mode shape comparison between XFEM (*left column*) and DNS (*right column*). Two modes at point Γ across the band gap are selected, as denoted in Fig. 2. The displacement at point A is enlarged by a factor of 2, while the mode shape at point B is reduced by a factor of 0.5. The mode shapes are colored according to the magnitude of displacement u_m

Table 3 Correspondence between radius and filler volume fraction of simple cubic crystals

Radius (mm)	5.0	5.8	6.64	6.99	7.31
Volume fraction (%)	12.8	20.0	30.0	35.0	40

stay unchanged. On the contrary, the geometry and mesh should be updated in the traditional FEM simulation (DNS) when the particle size varies. Therefore, the XFEM offers a convenient way to model the metamaterials with different microstructures, especially during the design and optimization process of the metamaterials, where the microstructures evolves with new iterations. In a typical topology optimization process hundreds or thousands iterations are required, leading to a substantial computational costs in re-building and re-meshing procedure in traditional DNS calculations.

4 Numerical examples

4.1 Face centered cubic (FCC) and body centered cubic (BCC) crystals

The band structure of mechanical metamaterials can be affected by the crystal lattice of embedded particles. Instead of using the SC crystal, we also consider the BCC and FCC

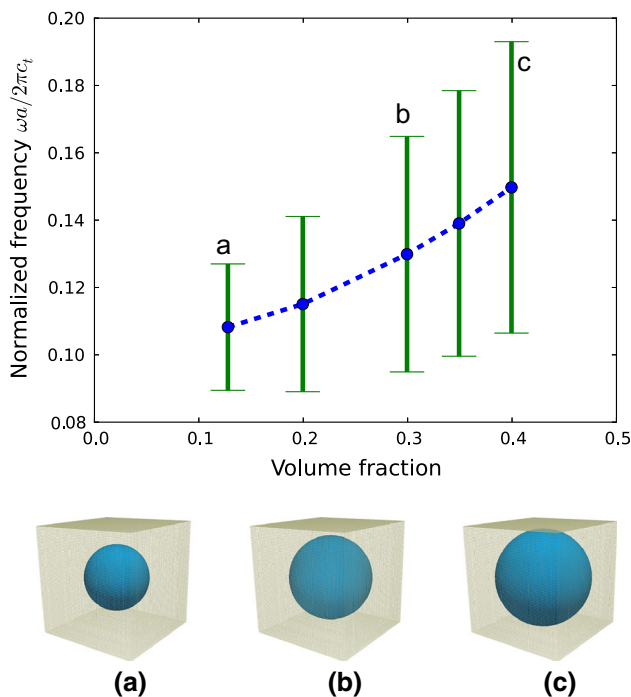


Fig. 5 Band gap dependence of filling volume fraction for SC crystals (*top*). The blue dots and error bars denote the location and width of the band gaps, respectively. The same uniform finite element meshes are used (*bottom*), regardless of the changing of particle radius, which illustrates the flexibility of XFEM formulation in modeling evolving geometries

crystals with material properties set to be the same as those of the SC crystal (cf. Table 1). The lattice constant is 16 mm and the spherical particle radius is fixed at 5 mm. $80 \times 80 \times 80$ are the dimensions of the uniform meshes used for both structures. According to different irreducible Brillouin zones of these crystals, 60 and 40 equally divided wave vectors are used to represent the boundaries of irreducible Brillouin zones (see Fig. 13) for FCC and BCC crystals, respectively. Their band structures are given in Figs. 6 and 7. The volume fractions of embedded particles in SC, BCC and FCC crystals are 12.78, 25.57 and 51.13 %, respectively. Therefore, the band gap width gradually increases from the SC lattice, followed by the BCC lattice, then the FCC lattice.

4.2 Local resonant phononic crystal (LRPC)

In the above cases, all of the band gaps are induced by the scattering of the longitudinal wave, due to the periodic variations of the density and modulus in the space. Thus, the lattice constant is required to be on the same order as the longitudinal wave length. When the band gap is desired in the low frequency range, i.e. below 1 kHz, the corresponding wave length will be several meters. Therefore, the length scale of the building block will be extremely large, preventing the real application of these metamaterials in this frequency range.

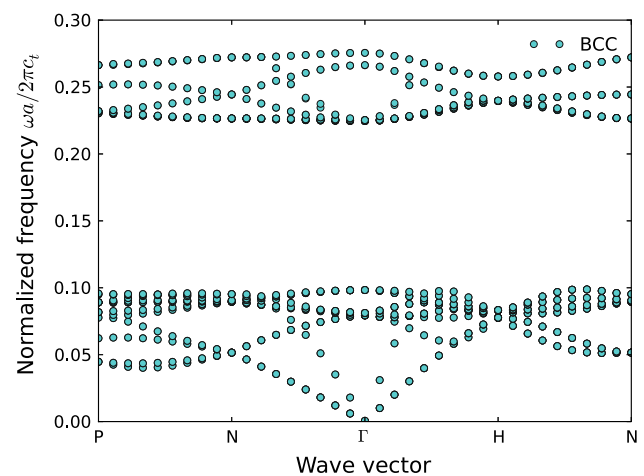


Fig. 6 Band gap structure of BCC crystal predicted by XFEM

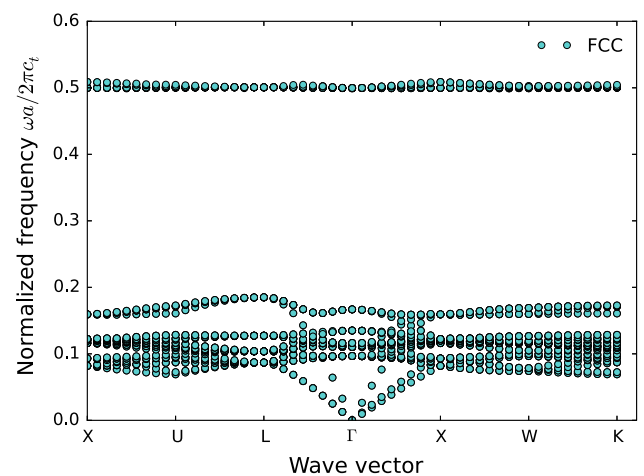


Fig. 7 Band gap structure of FCC crystal predicted by XFEM

To overcome this issue, Liu et al. proposed a new mechanism to excite low frequency acoustic band gaps by introducing a local resonant mode [36]. In this case, a three-phase composite material has been constructed by adding a softer interphase layer between the hard core and soft matrix. For instance, a lead sphere, coated by a thin layer of silicone rubber, is embedded into an epoxy matrix. The soft interphase provides space for the hard core to be excited into local resonant modes at a much lower frequency than the value predicted by the Bragg's scattering theory [36]. Essentially, these local vibration modes introduce a negative dynamic effective density around the resonant frequency [22,38], leading to an exponential wave attenuation and hence a complete forbidden gap. The discovery of the local resonant mode opens a new way to create the low frequency band gap by a completely different mechanism than the classical Bragg's scattering theory. The negative effective density induced low band gap frequency further inspires a substantial body of research in the field of mechanical metamaterials.

Table 4 Material properties for local resonant phononic crystals. E , ρ and ν are the Young's modulus, density and Poisson's ratio of the materials, respectively. c_l and c_t are the longitudinal and transverse speed of sound in the material $c_l = \sqrt{(\lambda + 2G)/\rho}$ and $c_t = \sqrt{G/\rho}$, where λ and G are Lamé first constant and shear modulus determined by E and ν

Materials	E (MPa)	ν	ρ (kg/m ³)	c_l (m/s)	c_t (m/s)
Lead (core)	4.082×10^4	0.37	11.6×10^3	2493.1	1133.4
Silicone rubber (interphase)	0.118	0.469	1.3×10^3	22.87	5.55
Epoxy (matrix)	4.35×10^3	0.368	1.18×10^3	2539.5	1160.8

Fang et al. demonstrated a system of Helmholtz resonators with negative modulus based on the idea of local resonance [18]. Later, a new class of mechanical metamaterials with simultaneously negative dynamic effective bulk modulus and mass density, in analogy to optical metamaterials with both negative permittivity and permeability, were discovered [13,30,33,34]. These double-negative metamaterials provide important applications in achieving negative refractive indexes and superlensing beyond the diffraction limit.

Here we apply the XFEM to numerically study the local resonant band gap of the three-phase composite material system. The geometric configuration of a unit cell is given in Fig. 9, consisting of a spherical lead particle coated by a thin silicone rubber layer and the epoxy matrix. The lattice constant of the unit cell is 15.5 mm with the lead particle having a radius 5 mm. The thickness of the silicone rubber is 2 mm. All of the material constants are summarized in Table 4, which are taken from the previous experimental study [36]. The band gap structure of the three-phase metamaterial is given in Fig. 8a. Comparing the band structures given in Figs. 8a and 2, the most distinct difference is that the dis-

persion curves of the local resonant crystal are characterized by a flat plateau, which indicates the existence of localized vibration mode. This is further confirmed by experimental evidence where wave transmission coefficient exhibits valley (cf. Fig. 8b) at the frequency near the local resonant mode, i.e. the grey region shown in Fig. 8a. At the end, the band gap frequency of the local resonant crystal is about 0.015–0.025, with the corresponding wave length much larger than the lattice constant.

Figure 9 shows the local resonant modes on the boundaries of the band gap at the Γ point. At the lower frequency point A (cf. Fig. 8), the lead particle exhibits rigid body motion with moderate elastic deformation. Such a behavior can be understood in analogy to a spring-mass system, where the hard particle and interphase layer behave like the heavy mass and soft spring, respectively. At higher frequency point B, most of the deformation occurs in the interphase region while the core and matrix are nearly stationary. These resonant behaviors are excited locally and immune from the outside wave vectors to some extent, which explains why the dispersion curve is \mathbf{K} -independent as a flat band structure. From a mathematical point of view, the localized resonant behavior leads to a negative dynamic effective density [22,30,38,61] followed by an exponential wave attenuation, hence resulting in a complete band gap.

4.3 Material with three-intersecting cylinders

To demonstrate the capability of the proposed method in handling complex microstructures, we design a two-phase material with three cylinders intersecting with each other (see Fig. 10). In the DNS model, the finite element mesh of the designed structure with tetrahedron elements is very complex and a tremendous number of elements should be used to resolve the boundaries between the intersecting cylinders,

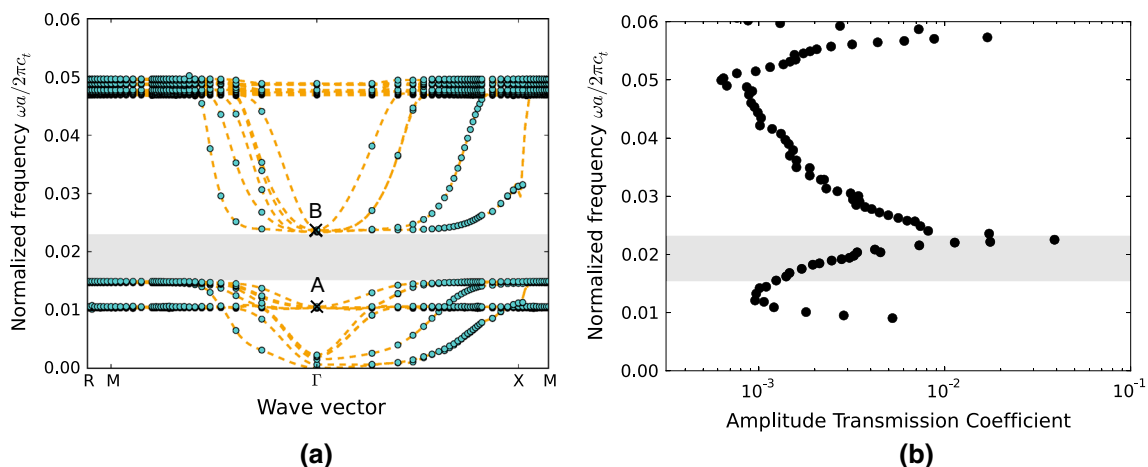


Fig. 8 **a** Band gap structure of local resonant phononic crystal predicted by XFEM and **b** experimental wave transmission coefficient given by Liu et al. [36]

Fig. 9 Configuration for the three-phase local resonant phononic crystal (*left*) and mode shapes at points A and B (*right*) as denoted in Fig. 8. Mode shapes at points A and B are enlarged by a factor of 2 and 5, respectively. The mode shapes are *colored* according to the displacement along y direction u_y

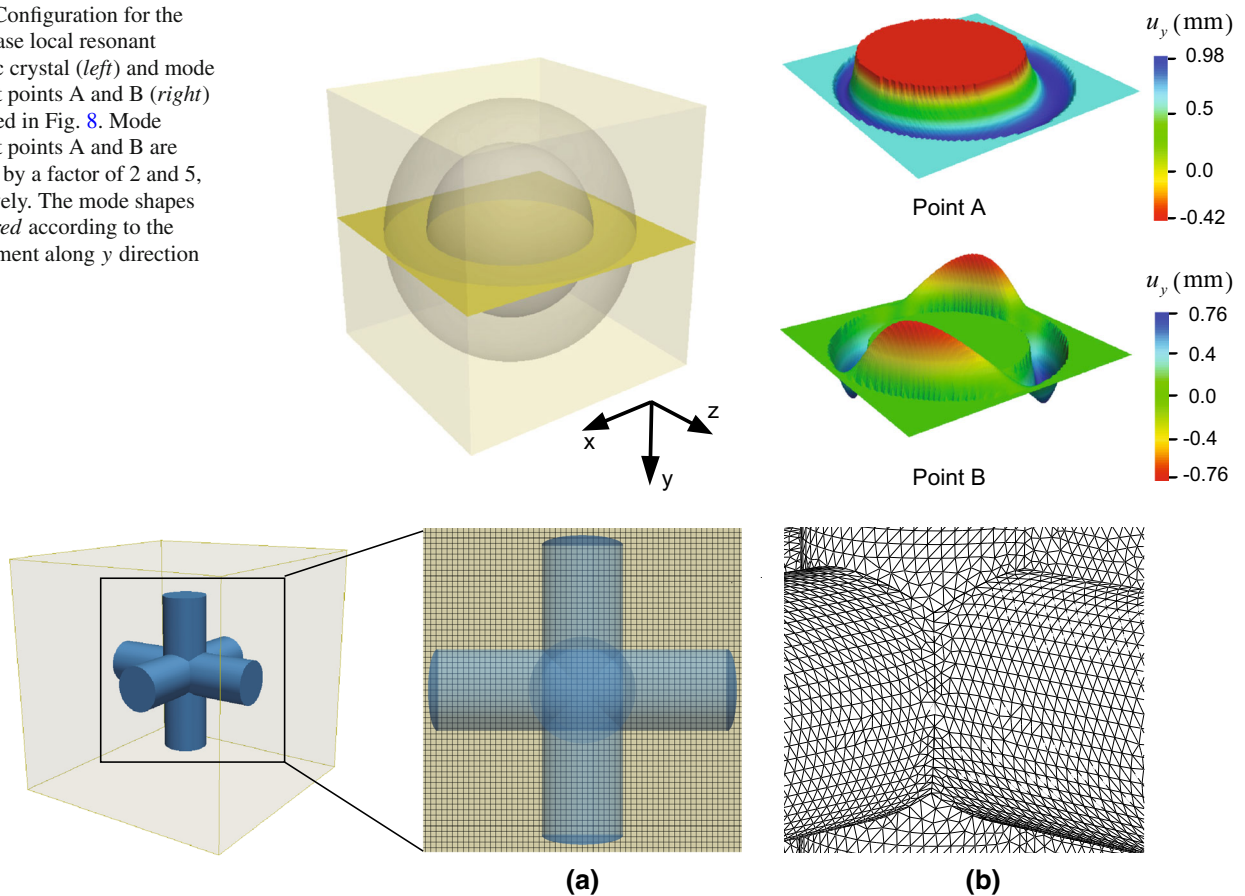


Fig. 10 Finite element meshes for **a** XFEM simulation and **b** transitional FEM. In traditional FEM, elements have to be aligned with geometry of the inclusion. XFEM, instead, is characterized with uniform finite element meshes

as shown in Fig. 10b. However, with the help of the level-set functions in XFEM, the previous $80 \times 80 \times 80$ uniform finite element meshes are ready to be used for resolving the complex geometry. The material properties are kept the same as that given in Table 1. The lattice constant is $a = 16$ mm, the cylinder radius is $r = 1.5$ mm, and the length of each cylinder is $l = 10.66$ mm. The three intersecting cylinders are arranged on a simple cubic lattice in the 3D space, with the irreducible Brillouin zone given in Fig. 13.

The band structure of the designed material is given in Fig. 11. Compared with the band structure shown in Fig. 2, there is no band gap observed, demonstrating the important role played by the geometry of embedded particles. As discussed before, the band gaps observed in these materials are induced by Bragg's scattering. When the shape of the embedded particle is spherical with high symmetry, the scattered longitudinal waves cancel each other out, resulting in the band gap. However, when the shape of the embedded particle becomes irregular with low symmetry, the scattered waves do not interfere with each other as much, as demonstrated in the mode shapes given in Fig. 12. Therefore, we cannot observe the band gap structure in these materials.

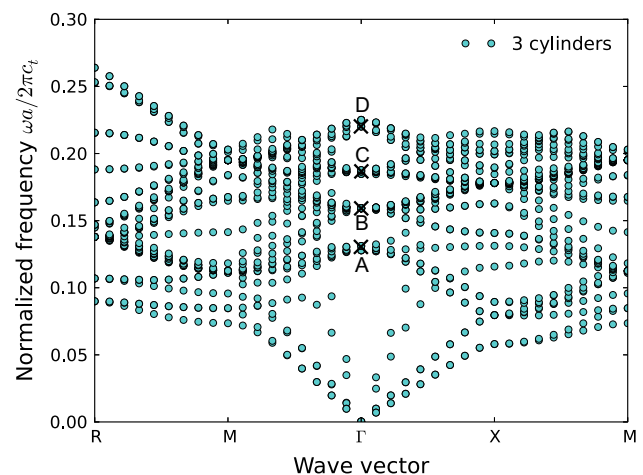


Fig. 11 Band structure for the two-phase material with three intersecting cylinders predicted by XFEM

5 Conclusions

In this study, a new computational approach has been proposed to predict the band gap structure of 3D mechanical metamaterials with complex microstructures based on the XFEM formulation. The proposed method has been vali-

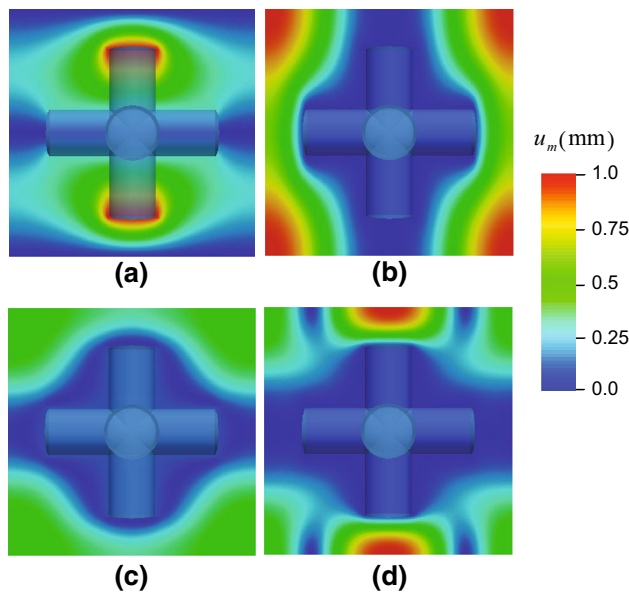


Fig. 12 Mode shapes of the four points denoted in Fig. 11 at point Γ . Mode shapes **a–d** correspond to the points *A, B, C, D* in Fig. 11, respectively

dated and verified through a simple problem with a spherical particle embedded in the center of a cube. The predicted band structure is found to be in excellent agreement with the result given by DNS. The mesh convergence of the new method is also demonstrated using this problem setup. A series of numerical examples in 3D with different microstructures have been solved using this method, demonstrating the flexibility and accuracy of the XFEM approach.

Comparing the XFEM with traditional FEM (DNS), the major advantage of this new method is the simplicity of defining the microstructure. A uniform mesh can be used on these materials, regardless of the geometry of the embedded particle, which is implicitly represented by the level-set function in the XFEM formulation. The utilization of a uniform mesh provides a prevailing advantage over DNS when dealing with complex geometries. More specifically, during the optimizing process the mesh of the current method does not need to be updated with the evolving microstructure, which can dramatically reducing the computational cost by removing the necessity for re-meshing. The simplicity of defining and changing the metamaterial microstructure using the proposed method opens new opportunities in structural optimization of mechanical metamaterials where evolving geometries are encountered.

We also emphasize that the proposed method still requires a relatively fine mesh on the same order of magnitude of DNS to obtain an accurate solution. However, this problem can be resolved by using the adaptivity mesh-refinement techniques [46, 62]. In this context, h-adaptive technique has been developed for meshfree method by Rabczuk and Belytschko [46]. In the classical finite element framework, the implementation

of adaptivity algorithm is more difficult [5], since removing and adding nodes/particles is not an easy task as that in mesh-free method. Recently, an excellent solution has been developed by Yuan et al. [62], which creates a robust and efficient mesh-refinement algorithm suitable for XFEM. In addition, we should also emphasize that the curved interface is only approximately represented by the first-order XFEM/level-set function in current study, which also sets the limit that the element size should be small enough. As pointed out by Cheng and Fries [10], higher-order shape functions will give better representation of the curved interface, but dose not necessarily lead to optimal convergence rate. Babuška and Banerjee have proposed a generalized finite element method [3], which can give better convergence rate by improving the conditioning of the stiffness matrix. More recently, iso-geometric analysis has been combined with XFEM to accurately capture the curved geometry [25]. All these works can be incorporated in our future study to improve the proposed method for designing mechanical metamaterials.

Acknowledgments We are grateful to Dr. Hong Zhang from Argonne National Laboratory for helpful discussions on how to use PETSc and SLEPc. We express thanks to Jacob Smith from Northwestern University for revising English for this paper. Y.L. warmly expresses thanks for the financial support provided by Ryan Fellowship and Royal E. Cabell Terminal Year Fellowship, as well as a supercomputing grant on Quest from Northwestern University High Performance Computing Center. W.K.L. expresses thanks for the support from AFOSR Grant No. FA9550-14-1-0032.

Appendix 1: Reciprocal lattice and Brillouin zone

Suppose a periodic structure is characterized by a spatial translation vector \mathbf{T}

$$\mathbf{T} = n_i \mathbf{a}_i \quad (25)$$

where n_i is an arbitrary integer and \mathbf{a}_i are primitive vectors as in Eq. 5. The reciprocal lattice is then defined as a set of vectors \mathbf{G} that satisfy

$$\exp(i\mathbf{G} \cdot \mathbf{T}) = 1 \quad (26)$$

for all possible lattice position vectors \mathbf{T} . Vector \mathbf{G} is also called a reciprocal vector.

For a three-dimensional problem, \mathbf{G} can be written as:

$$\mathbf{G} = p_i \mathbf{b}_i \quad (27)$$

where p_i is an arbitrary integer and \mathbf{b}_i are primitive vectors in reciprocal space defined as

$$\mathbf{b}_1 = 2\pi \frac{\mathbf{a}_2 \times \mathbf{a}_3}{\mathbf{a}_1 \cdot (\mathbf{a}_2 \times \mathbf{a}_3)} \quad (28)$$

$$\mathbf{b}_2 = 2\pi \frac{\mathbf{a}_3 \times \mathbf{a}_1}{\mathbf{a}_2 \cdot (\mathbf{a}_3 \times \mathbf{a}_1)} \quad (29)$$

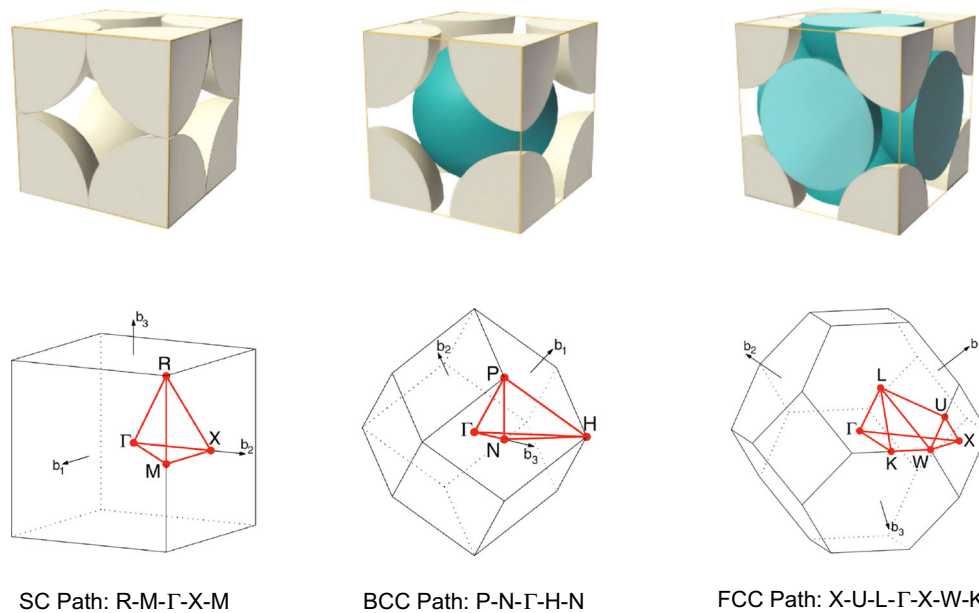


Fig. 13 Original lattice structures and corresponding irreducible Brillouin zones in the reciprocal space for SC, BCC and FCC crystals. The figure is adapted from Ref. [51]

$$\mathbf{b}_3 = 2\pi \frac{\mathbf{a}_1 \times \mathbf{a}_2}{\mathbf{a}_3 \cdot (\mathbf{a}_2 \times \mathbf{a}_1)} \quad (30)$$

Any vector that connects two points on the reciprocal lattice is a reciprocal vector. In plane wave propagation problems, Bloch wave vectors \mathbf{K} are in the reciprocal space.

Brillouin zone is the primitive cell in reciprocal space, analogous to the primitive cell in defining the spatial periodicity. For description of a Bloch wave in a periodic medium, the solutions for all the wave vectors in the reciprocal space can be completely characterized by the behavior in the single Brillouin zone. All Bloch wave vectors can be translated to the Brillouin zone by a reciprocal vector.

$$\mathbf{K} = \mathbf{K}' + \mathbf{G} \quad (31)$$

where \mathbf{K}' is the wave vector in the Brillouin zone.

Due to the symmetries, the Brillouin zone can be further reduced to an irreducible zone. Figure 13 shows the irreducible Brillouin zone for SC, BCC and FCC crystals.

Appendix 2: Solver options for PETSc and SLEPc

The equation to be solved (as in Eq. 18) is a generalized eigenvalue problem with symmetric and definite matrices. A typical example of a generalized eigensolver is available through [21]. The runtime keywords that can be used directly with the example eigensolver are summarized as:

```
“-eps_type krylovschur -eps_target 10.0 -st_ksp_type
minres -st_pc_type bjacobi -st_sub_pc_type icc -st_ksp_
rtol 1.e-4 -eps_tol 1.e-4 -eps_nev 40 -st_type sinvert”.
```

References

1. Ambati M, Fang N, Sun C, Zhang X (2007) Surface resonant states and superlensing in acoustic metamaterials. *Phys Rev B* 75(19):195–447
2. Axmann W, Kuchment P (1999) An efficient finite element method for computing spectra of photonic and acoustic band-gap materials: I. scalar case. *J Comput Phys* 150(2):468–481
3. Babuška I, Banerjee U (2012) Stable generalized finite element method (sgfem). *Comput Methods Appl Mech Eng* 201:91–111
4. Balaz S, Abhyankar S, Adams MF, Brown J, Brune P, Buschelman K, Eijkhout V, Gropp WD, Kaushik D, Knepley MG, McInnes LC, Rupp K, Smith BF, Zhang H (2014) PETSc users manual. Technical Report ANL-95/11 - Revision 3.5, Argonne National Laboratory
5. Belytschko T, Tabbara M (1993) H-adaptive finite element methods for dynamic problems, with emphasis on localization. *Int J Numer Methods Eng* 36(24):4245–4265
6. Belytschko T, Liu WK, Moran B, Elkhodary K (2013) Nonlinear finite elements for continua and structures. Wiley, Chichester
7. Biwa S, Yamamoto S, Kobayashi F, Ohno N (2004) Computational multiple scattering analysis for shear wave propagation in unidirectional composites. *Int J Solids Struct* 41(2):435–457
8. Cai W, Chettiar UK, Kildishev AV, Shalaev VM (2007) Optical cloaking with metamaterials. *Natu Photonics* 1(4):224–227
9. Chen H, Chan C (2007) Acoustic cloaking in three dimensions using acoustic metamaterials. *Appl Phys Lett* 91(18):183–518
10. Cheng KW, Fries TP (2010) Higher-order xfem for curved strong and weak discontinuities. *Int J Numer Methods Eng* 82(5):564–590
11. Cottrell J, Reali A, Bazilevs Y, Hughes T (2006) Isogeometric analysis of structural vibrations. *Comput Methods Appl Mech Eng* 195(41):5257–5296
12. Cottrell JA, Hughes TJ, Bazilevs Y (2009) Isogeometric analysis: toward integration of CAD and FEA. Wiley, Chichester
13. Ding Y, Liu Z, Qiu C, Shi J (2007) Metamaterial with simultaneously negative bulk modulus and mass density. *Phys Rev Lett* 99(9):093–904
14. Dobson DC (1999) An efficient method for band structure calculations in 2d photonic crystals. *J Comput Phys* 149(2):363–376

15. Dolbow J, Belytschko T (1999) A finite element method for crack growth without remeshing. *Int J Numer Methods Eng* 46(1):131–150
16. Eleftheriades GV, Balmain KG (2005) Negative-refraction metamaterials: fundamental principles and applications. Wiley, New York
17. Fang N, Lee H, Sun C, Zhang X (2005) Sub-diffraction-limited optical imaging with a silver superlens. *Science* 308(5721):534–537
18. Fang N, Xi D, Xu J, Ambati M, Srituravanich W, Sun C, Zhang X (2006) Ultrasonic metamaterials with negative modulus. *Nat Mater* 5(6):452–456
19. Fries TP (2008) A corrected xfm approximation without problems in blending elements. *Int J Numer Methods Eng* 75(5):503–532
20. Gonella S, To AC, Liu WK (2009) Interplay between phononic bandgaps and piezoelectric microstructures for energy harvesting. *J Mech Phys Solids* 57(3):621–633
21. Hernandez V, Roman JE, Vidal V (2014) SLEPc Web page. <http://www.grycap.upv.es/slep>
22. Huang H, Sun C, Huang G (2009) On the negative effective mass density in acoustic metamaterials. *Int J Eng Sci* 47(4):610–617
23. Hughes TJ, Cottrell JA, Bazilevs Y (2005) Isogeometric analysis: Cad, finite elements, nurbs, exact geometry and mesh refinement. *Comput Methods Appl Mech Eng* 194(39):4135–4195
24. Hussein MI (2009) Reduced bloch mode expansion for periodic media band structure calculations. *Proc R Soc A* 465(2109):2825–2848
25. Jia Y, Anitescu C, Ghorashi SS, Rabczuk T (2014) Extended isogeometric analysis for material interface problems. *IMA J Appl Math* p. hxu004
26. Jun S, Cho YS (2003) Deformation-induced bandgap tuning of 2d silicon-based photonic crystals. *Opt Express* 11(21):2769–2774
27. Jun S, Cho YS, Im S (2003) Moving least-square method for the band-structure calculation of 2d photonic crystals. *Opt Express* 11(6):541–551
28. Kittel C, McEuen P (1976) Introduction to solid state physics, vol 8. Wiley, New York
29. Kobayashi F, Biwa S, Ohno N (2004) Wave transmission characteristics in periodic media of finite length: multilayers and fiber arrays. *Int J Solids Struct* 41(26):7361–7375
30. Lai Y, Wu Y, Sheng P, Zhang ZQ (2011) Hybrid elastic solids. *Nat Mater* 10(8):620–624
31. Laude V, Wilm M, Benchabane S, Khelif A (2005) Full band gap for surface acoustic waves in a piezoelectric phononic crystal. *Phys Rev E* 71(3):036–607
32. Lee B, To A (2009) Enhanced absorption in one-dimensional phononic crystals with interfacial acoustic waves. *Appl Phys Lett* 95(3):031–911
33. Lee SH, Park CM, Seo YM, Wang ZG, Kim CK (2010) Composite acoustic medium with simultaneously negative density and modulus. *Phys Rev Lett* 104(5):054–301
34. Li J, Chan C (2004) Double-negative acoustic metamaterial. *Phys Rev E* 70(5):055–602
35. Liu WK, Li S, Belytschko T (1997) Moving least-square reproducing kernel methods (i) methodology and convergence. *Comput Methods Appl Mech Eng* 143(1):113–154
36. Liu Z, Zhang X, Mao Y, Zhu Y, Yang Z, Chan C, Sheng P (2000) Locally resonant sonic materials. *Science* 289(5485):1734–1736
37. Liu Z, Chan C, Sheng P (2002) Three-component elastic wave band-gap material. *Phys Rev B* 65(16):116–165
38. Liu Z, Chan C, Sheng P (2005) Analytic model of phononic crystals with local resonances. *Phys Rev B* 71(1):014–103
39. Martin A, Kadic M, Schittny R, Bückmann T, Wegener M (2012) Phonon band structures of three-dimensional pentamode metamaterials. *Phys Rev B* 86(15):116–155
40. Matsuki T, Yamada T, Izui K, Nishiwaki S (2014) Topology optimization for locally resonant sonic materials. *Appl Phys Lett* 104(19):191–905
41. Mei J, Ma G, Yang M, Yang Z, Wen W, Sheng P (2012) Dark acoustic metamaterials as super absorbers for low-frequency sound. *Nat Commun* 3:756
42. Milton GW, Cherkaev AV (1995) Which elasticity tensors are realizable? *J Eng Mater Technol* 117(4):483–493
43. Moës N, Cloirec M, Cartraud P, Remacle JF (2003) A computational approach to handle complex microstructure geometries. *Comput Methods Appl Mech Eng* 192(28):3163–3177
44. Pendry JB (2000) Negative refraction makes a perfect lens. *Phys Rev Lett* 85(18):3966
45. Qiu M, He S (2000) A nonorthogonal finite-difference time-domain method for computing the band structure of a two-dimensional photonic crystal with dielectric and metallic inclusions. *J Appl Phys* 87(12):8268–8275
46. Rabczuk T, Belytschko T (2005) Adaptivity for structured mesh-free particle methods in 2d and 3d. *Int J Numer Methods Eng* 63(11):1559–1582
47. Reissland J, Klemens PG (2008) The physics of phonons, vol 28. American Institute of Physics, College Park
48. Roman JE, Campos C, Romero E, Tomas A (2014) SLEPc users manual. Technical Report DSIC-II/24/02 - Revision 3.5, D. Sistemes Informàtics i Computació, Universitat Politècnica de València
49. Romero E, Roman JE (2014) A parallel implementation of davidson methods for large-scale eigenvalue problems in slepc. *ACM Trans Math Softw* 40(2):13
50. Sainidou R, Stefanou N, Modinos A (2002) Formation of absolute frequency gaps in three-dimensional solid phononic crystals. *Phys Rev B* 66(21):212–301
51. Setyawan W, Curtarolo S (2010) High-throughput electronic band structure calculations: challenges and tools. *Comput Mater Sci* 49(2):299–312
52. Sigalas M, Garcia N (2000) Theoretical study of three dimensional elastic band gaps with the finite-difference time-domain method. *J Appl Phys* 87(6):3122–3125
53. Soukoulis CM (2001) Photonic crystals and light localization in the 21st century, vol 563. Springer, New York
54. Sukumar N, Pask J (2009) Classical and enriched finite element formulations for bloch-periodic boundary conditions. *Int J Numer Methods Eng* 77(8):1121–1138
55. Tian R, To AC, Liu WK (2011) Conforming local meshfree method. *Int J Numer Methods Eng* 86(3):335–357
56. Wang Y, Li F, Wang Y, Kishimoto K, Huang W (2009) Tuning of band gaps for a two-dimensional piezoelectric phononic crystal with a rectangular lattice. *Acta Mech Sin* 25(1):65–71
57. Wang Y, Luo Z, Zhang N, Kang Z (2014) Topological shape optimization of microstructural metamaterials using a level set method. *Comput Mater Sci* 87:178–186
58. Wu TT, Huang ZG, Lin S (2004) Surface and bulk acoustic waves in two-dimensional phononic crystal consisting of materials with general anisotropy. *Phys Rev B* 69(9):094–301
59. Yablonovitch E, Gmitter T (1989) Photonic band structure: the face-centered-cubic case. *Phys Rev Lett* 63(18):1950
60. Yao J, Liu Z, Wang Y, Sun C, Bartal G, Stacy AM, Zhang X (2008) Optical negative refraction in bulk metamaterials of nanowires. *Science* 321(5891):930–930
61. Yao S, Zhou X, Hu G (2008) Experimental study on negative effective mass in a 1d mass-spring system. *New J Phys* 10(4):20–43
62. Yuan R, Singh SS, Chawla N, Oswald J (2014) Efficient methods for implicit geometrical representation of complex material microstructures. *Int J Numer Methods Eng* 98(2):79–91

63. Zhang H, Smith B, Sternberg M, Zapol P (2007) Sips: shift-and-invert parallel spectral transformations. *ACM Trans Math Softw* 33(2):9
64. Zhang P, To AC (2013) Broadband wave filtering of bioinspired hierarchical phononic crystal. *Appl Phys Lett* 102(12):121–910
65. Zhao H, Liu Y, Wang G, Wen J, Yu D, Han X, Wen X (2005) Resonance modes and gap formation in a two-dimensional solid phononic crystal. *Phys Rev B* 72(1):012–301
66. Zhou F, Bao Y, Cao W, Stuart CT, Gu J, Zhang W, Sun C (2011) Hiding a realistic object using a broadband terahertz invisibility cloak. *Sci Rep* 1:78